The Journal of Chemical Physics

RESEARCH ARTICLE | MARCH 18 2025

Reaction-limited evaporation for the color-gradient lattice Boltzmann model

Gaurav Nath ; Othmane Aouane ; Jens Harting

J. Chem. Phys. 162, 114110 (2025)
https://doi.org/10.1063/5.0253799

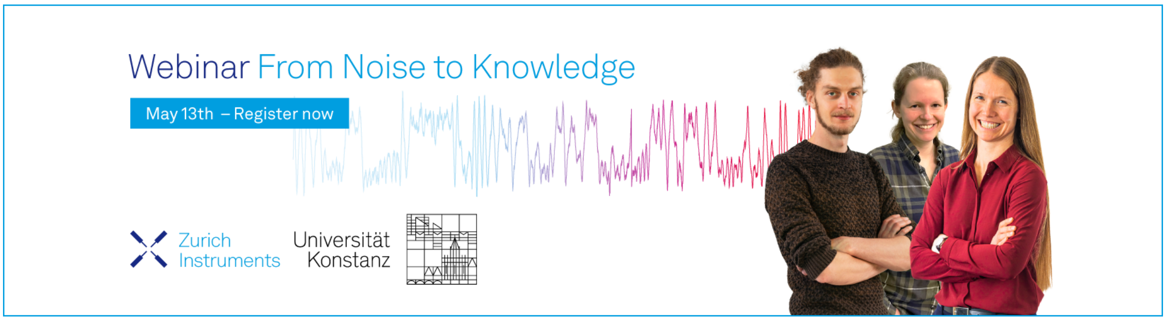

AIP Publishing

The Journal of Chemical Physics ARTICLE pubs.aip.org/aip/jcp

Reaction-limited evaporation for the color-gradient lattice Boltzmann model

Cite as: J. Chem. Phys. 162, 114110 (2025); doi: 10.1063/5.0253799
Submitted: 19 December 2024 • Accepted: 24 February 2025 •
Published Online: 18 March 2025

View Online Export Citation CrossMark

Gaurav Nath,[1,a)] **Othmane Aouane,**[1,b)] **and Jens Harting**[1,2,c)]

AFFILIATIONS

[1] Helmholtz Institute Erlangen-Nürnberg for Renewable Energy, Forschungszentrum Jülich, Cauerstr. 1, 91058 Erlangen, Germany
[2] Department of Chemical and Biological Engineering and Department of Physics, Friedrich-Alexander-Universität Erlangen-Nürnberg, Cauerstr. 1, 91058 Erlangen, Germany

[a)] **Email:** n.gaurav@fz-juelich.de
[b)] **Email:** o.aouane@fz-juelich.de
[c)] **Author to whom correspondence should be addressed:** j.harting@fz-juelich.de

ABSTRACT

We propose a reaction-limited evaporation model within the color-gradient lattice Boltzmann (LB) multicomponent framework to address the lack of intrinsic evaporation mechanisms. Unlike diffusion-driven approaches, our method directly enforces mass removal at the fluid interface in a reaction-limited manner while maintaining numerical stability. Using the inherent color-gradient magnitude and a single adjustable parameter, evaporation sites are chosen in a computationally efficient way with seamless mass exchange between the components, with no change to the core algorithm. Extensive validation across diverse interface geometries and evaporation flux magnitudes demonstrates high accuracy, with errors below 5% for unit density ratios. For density contrasts, the method remains robust in the limit of smaller evaporation flux magnitudes and density ratios. Our approach extends the applicability of the color-gradient LB model to scenarios involving reaction-limited evaporation, such as droplet evaporation on heated substrates, vacuum evaporation of molten metals, and drying processes in porous media.

I. INTRODUCTION

Evaporation can occur in different regimes, specifically diffusion-limited (DL) and reaction-limited (RL), depending on the governing mechanism. In the diffusion-limited regime, vapor molecules move away from the liquid–vapor interface due to diffusion. This regime is commonly observed when evaporation occurs in a still mixture of gases and is often chosen for studying evaporation in droplets.[1–8] However, in scenarios such as evaporation in a vacuum, a pure vapor phase, or in the presence of a gas draft, the DL regime may not be applicable.[9] In such cases, the RL regime, where the transfer rate of molecules across the liquid–vapor interface is the limiting mechanism, should be considered.

RL evaporation plays a crucial role in various applications. It is considered in continuum models for drying in porous media,[10,11] with applications in soil water evaporation[12] and water evaporation in polymer electrolyte fuel cells.[13] RL evaporation is also utilized in studying the evaporation of molten metals, such as in the vacuum refining of Manganese (Mn) steel melts[14] and the vacuum evaporation of pure metals, such as titanium and zirconium, at high temperatures in rarified environments.[15] Additionally, in the context of drop evaporation, the RL regime is significant for the evaporation of micro-drops of pure liquids[16] and for drop evaporation from heated substrates.[3,17,18]

The Hertz–Knudsen (HK) relation,[19,20] based on the kinetic theory of gases, is often used to model the local mass flux ϕ, leaving the interface in RL evaporation. Using the Clausius–Clapeyron law, the HK relation can be expressed as

$$\phi = \frac{\Lambda\, \rho_v\, \mathscr{L}}{T_{sat}^{3/2}} \sqrt{\frac{M_v}{2\pi R_g}}\, [T_i - T_{sat}]. \tag{1}$$

Here, $0 \le \Lambda \le 1$ represents the accommodation coefficient (a measure of liquid volatility), M_v is the molecular mass of the vapor, ρ_v is the density of the vapor, R_g is the universal gas constant,

$\mathscr{L}$ is the latent heat of vaporization, T_i is the interface temperature (assumed to be continuous across the interface), and T_{sat} is the saturation temperature. The difference between T_{sat} and T_i drives the flux. Despite known limitations,[21] the HK relation's simplicity has led to extensive use in theoretical works on droplet evaporation.[3,8,17,18,22,23] It has been adopted for the non-equilibrium one-sided (NEOS) model for evaporation due to its capability of decoupling the drop dynamics from the vapor side.[24] In this work, we adopt a similar approach for Lattice Boltzmann (LB) simulations.

Among the different classes of LB multicomponent models,[25] the color-gradient (CG) approach[26,27] has found widespread application in studying two-phase flows in porous media,[28–30] thermo-capillary flows,[31–33] and microfluidic applications.[34,35] Its strength lies in achieving large kinematic viscosity ratios (up to 1000)[25] and independent tuning of crucial parameters, such as surface tension and interface thickness.[36] In recent years, several works[36–40] have improved the CG model, making it viable for general three-dimensional multiphase/multicomponent flows and overcoming the limitations of the previous implementations. However, unlike the pseudo-potential[41] (PP) and free-energy[42] (FE) based multicomponent models, the CG model does not have an inherent method of achieving evaporation. The multicomponent PP and FE methods are well-known for exhibiting diffusion-limited evaporation[43,44] and are subsequently used for drying applications.[45–50] The CG model does not exhibit similar diffusion behavior as it is intended for immiscible fluids.

Additionally, the CG model uses an isothermal equation of state that does not account for phase change. Aursjø and Pride[51] proposed an LB model for two partially miscible fluids where the fluid has two distinct regions—an interfacial region where color separation and surface tension are enforced and a miscible region where an advection–diffusion equation governs concentrations. Subsequently, they demonstrated the dissolution of one fluid component into another while maintaining a freely moving interface. The model shares CG features and could be adopted for diffusion-limited evaporation but introduces the complication of solving two different algorithms in complementary fluid regions (interface and bulk). Another approach used in the CG literature[52,53] is to convert one fluid component into the other (red to blue) at the domain's boundaries. However, the said conversion cannot be considered evaporation as it does not obey any evaporation regimes. Considering the above literature, there is a need for a straightforward evaporation method in the CG model. Considering the limitations of the CG model with diffusion-limited evaporation, we propose a novel way to achieve reaction-limited evaporation. Unlike the diffusion-driven approaches of PP and FE models, the current method directly enforces mass removal at the fluid interface in a reaction-limited manner. Additionally, it involves a low computational overhead and no change to the core CG algorithm. This extends the usability of CG models to scenarios involving reaction-limited evaporation. To the best of the authors' knowledge, this approach has not been attempted before in the CG framework.

In RL evaporation, the rate of mass loss is directly related to the liquid–vapor surface area. The proposed method involves removing fluid mass from the lattice sites in the interface region formed between the fluid components. We have developed a consistent way of selecting these evaporation sites based on the calculated color-gradient magnitude and a threshold value (free parameter). The threshold, which depends on a given set of CG model parameters, is chosen through a series of benchmarks. As a result, the current method can yield results consistent with RL evaporation.

The remaining sections of this paper are organized as follows: Sec. II explains the CG model and the RL evaporation algorithm, while Sec. III presents benchmarks and discusses the strategy for choosing the free parameter. Finally, Sec. IV summarizes the findings and explores potential use cases of the current method.

II. SIMULATION METHOD

A. Color-gradient lattice Boltzmann multicomponent model

In this work, we adopt the generalized three-dimensional color-gradient (CG) model proposed by Leclaire *et al.*[36] For a given fluid component k, $f_i^k(\boldsymbol{x},t)$ represents the density of particles at site $\boldsymbol{x}$ at time t moving along the link direction i with velocity $\boldsymbol{c}_i$. A *color-blind distribution function* is then defined as $f_i = \sum_k f_i^k$ with the component density, total fluid density, and color-blind population velocity given by $\rho_k = \sum_i f_i^k$, $\rho = \sum_k \rho_k$, and $\boldsymbol{u} = \frac{1}{\rho}\sum_i f_i \boldsymbol{c}_i$, respectively. The collision step is performed on the color-blind population via the BGK[54] (Bhatnagar–Gross–Krook) single relaxation time collision operator (Ω_{BGK}), given by

$$\Omega_{BGK}(f_i) = f_i - \frac{\Delta t}{\tau}\left[f_i - f_i^{eq}\right]. \tag{2}$$

Here, τ is the effective relaxation time determined from the harmonic density weighted average of the component relaxation times (τ_k) as $\frac{1}{\tau} = \sum_k \frac{\rho_k}{\rho}\frac{1}{\tau_k}$. The component viscosity ν_k is defined as $\nu_k = c_s^2(\tau_k - \frac{\Delta t}{2})$, where c_s is the lattice speed of sound, and the equilibrium distribution function f_i^{eq}, based on a Maxwellian distribution, is given by

$$f_i^{eq}(\rho,\boldsymbol{u}) = \rho\left[A_i + B_i\bar{\alpha} + W_i\left(3(\boldsymbol{c}_i\cdot\boldsymbol{u}) + \frac{9}{2}(\boldsymbol{c}_i\cdot\boldsymbol{u})^2 - \frac{3}{2}(\boldsymbol{u}\cdot\boldsymbol{u})\right)\right]. \tag{3}$$

A_i, B_i, and W_i are lattice-specific weights and can be found in Ref. 36. Parameter $\bar{\alpha}$ is introduced to account for the density ratio (γ) between fluid components and is determined using the arithmetic density weighted average of the component free parameters (α_k) as $\bar{\alpha} = \sum_k \frac{\rho_k}{\rho}\alpha_k$. The least dense fluid component is assigned $\alpha_k = W_0$ and $\alpha_k = 1 - \frac{[1-W_0]}{\gamma_k}$ is used for the rest, where $\gamma_k = \rho_k^{in}/\rho_{\min}^{in}$ is the ratio of the initial densities of a given component k to the least dense component. The pressure in each homogeneous region is then given by

$$p_k = \rho_k\zeta[1-\alpha_k], \tag{4}$$

where ζ is a lattice dependent weight,[36] related to the isothermal speed of sound $(c_s^k)^2$.

A perturbation operator (Ω_{pert})[26,55] is used to enforce surface tension in the CG model. It is given by

$$\Omega_{pert}(f_i) = f_i + \sum_r \sum_{b=r+1} \frac{9}{4}\frac{\sigma_{rb}}{\tau}\left|\boldsymbol{F}_{rb}\right|\left[W_i\frac{(\boldsymbol{F}_{rb}.\boldsymbol{c}_i)^2}{\left|\boldsymbol{F}_{rb}\right|^2} - C_i\right], \tag{5}$$

where C_i is a lattice dependent weight.[36] For a given pair of fluid components (ρ_r, ρ_b) having surface tension σ_{rb}, $\boldsymbol{F}_{rb}$ is the color-gradient defined as

$$\boldsymbol{F}_{rb} = \nabla\left(\frac{\rho_r - \rho_b}{\rho_r + \rho_b}\right). \tag{6}$$

A recoloring operator (Ω_{recol}) is then used to recover the component populations from the color-blind population,

$$f_i^{r*} \equiv \Omega^r_{recol}(f_i) = \frac{\rho_r}{\rho} f_i + \sum_{\substack{b \\ b\neq r}} \beta \frac{\rho_r \rho_b}{\rho^2} \cos(\vartheta_{rb})\, f_i^{eq}(\rho, 0), \tag{7}$$

where $0 \leq \beta \leq 1$ controls the interface thickness and ϑ_{rb} is the angle between the color-gradient vector $\boldsymbol{F}_{rb}$ and lattice velocity vector $\boldsymbol{c}_i$.

After the above operations (collision → perturbation → recoloring), the resulting distribution functions f_i^{k*} are then streamed to the neighboring lattice nodes, completing one timestep,

$$f_i^k(\boldsymbol{x} + \boldsymbol{c}_i \Delta t, t + \Delta t) = f_i^{k*}(\boldsymbol{x}, t). \tag{8}$$

We use a D3Q19 lattice in the current work $(i = 0\text{–}18)$, and the lattice spacing Δx and timestep Δt are taken to be unity in respective lattice units.

The gradient of the color function $\rho^N = \left(\frac{\rho_r - \rho_b}{\rho_r + \rho_b}\right)$ is calculated via a compact finite difference scheme, given as

$$\frac{\partial \rho^N(\boldsymbol{x})}{\partial x_\alpha} = \frac{1}{c_s^2} \sum_i W_i\, \rho^N(\boldsymbol{x} + \boldsymbol{c}_i)\, \boldsymbol{c}_{i\alpha}. \tag{9}$$

B. Reaction-limited evaporation

In reaction-limited evaporation, the total mass loss rate (dM/dt) is directly proportional to the surface area of the evaporating liquid, denoted as A_S, and can be expressed as

$$\frac{dM}{dt} = -\iint_{A_S} \phi\, dA_S, \tag{10}$$

where ϕ represents the scalar mass flux normal to the elemental area dA_S, and is considered a constant in this context.

In lattice Boltzmann (LB) simulations, mass removal must be accounted for at the interface region between fluid components, referred to as evaporation sites $(\boldsymbol{x} \in \boldsymbol{x}_I)$. At each discrete evaporation site, an elementary volume of $(\Delta x)^3$, where Δx is the lattice spacing, can be assumed. The combined mass flux leaving through its faces can be set as ϕ. This allows for the re-expression of Eq. (10) for discrete evaporation sites in LB as

$$\frac{dM}{dt} = -\iint_{A_S} \phi\, dA_S = -S \sum_{\boldsymbol{x} \in \boldsymbol{x}_I} \phi (\Delta x)^2. \tag{11}$$

Here, S represents a correction factor (a real-valued constant) introduced to account for errors resulting from the discretization of the fluid interface on a lattice, which will be further discussed later. The total mass change can also be attributed to a mass sink with rate $\varphi = d\rho/dt$ (a constant) in each elementary volume, leading to the following relations:

$$\frac{dM}{dt} = -S \sum_{\boldsymbol{x} \in \boldsymbol{x}_I} \phi (\Delta x)^2 = -\sum_{\boldsymbol{x} \in \boldsymbol{x}_I} \varphi (\Delta x)^3, \tag{12}$$

$$\phi = \bar{S}\, \varphi\, \Delta x \quad \left[\bar{S} = \frac{1}{S}\right]. \tag{13}$$

Consequently, achieving an evaporation rate similar to reaction-limited evaporation with mass flux ϕ can be realized by removing fluid mass from evaporation sites at a rate of φ, following the relation in Eq. (13). In LB, $\varphi \Delta t$ represents the fluid mass to be removed per unit volume of an evaporation site in one timestep Δt. The mass exchange between the resting populations of the evaporating and surrounding fluid components is described as follows:

$$\begin{aligned} f_0^r(\boldsymbol{x}, t)^{\text{new}} &= f_0^r(\boldsymbol{x}, t) - \varphi \Delta t \\ f_0^b(\boldsymbol{x}, t)^{\text{new}} &= f_0^b(\boldsymbol{x}, t) + \varphi \Delta t \end{aligned} \qquad \forall\ \boldsymbol{x} \in \boldsymbol{x}_I. \tag{14}$$

The above equation adjusts the individual component densities (ρ_r, ρ_b), while the total density (ρ) at a site remains unaffected. Consequently, the method is globally mass-conserving and does not affect momentum.

The sites where evaporation occurs $(\boldsymbol{x} \in \boldsymbol{x}_I)$ can be determined using the color-gradient magnitude $\|\boldsymbol{F}_{rb}\|$ between two fluid components. This magnitude varies from zero in bulk to a maximum value near the interface region, as illustrated in Fig. 1(a). A threshold (Γ) can then be applied to select evaporation sites at the interface based on the criterion

$$\|\boldsymbol{F}_{rb}\| > \Gamma. \tag{15}$$

Here, Γ is a specified constant set at the beginning of the simulation and remains unchanged throughout. The selection of Γ determines the value of the real-valued correction factor $\bar{S} = 1/S$. For simplicity, $\bar{S}$ is assumed to be a natural number constant. The optimal value of Γ is determined by ensuring that the total mass loss rate is equal in both the LB simulation and the analytical solution, i.e., Eq. (11) is satisfied. The position of the interface during evaporation is compared between the LB simulations and analytical solutions. Figures 1(b), 1(c), and 1(d) display the evaporation sites selected at the fluid interface for $\bar{S} = 3$, 2, and 1, along with their corresponding Γ, for an evaporating spherical drop with unit density ratio and $\beta = 0.99$.

From Fig. 1, it can be inferred that $\bar{S}$ roughly represents the number of layers of evaporation sites selected at the interface. However, if $\bar{S}$ is not carefully chosen, holes may appear in the selected layer, as shown in Fig. 1(d) for $\bar{S} = 1$. To avoid this issue, it is recommended to choose $\bar{S} > 1$.

The overall method is summarized as follows:

1. Given a flux ϕ and a chosen $\bar{S}$, the mass sink rate φ is determined using Eq. (13).
2. The evaporation sites $(\boldsymbol{x} \in \boldsymbol{x}_I)$ for a given pair of fluid components are chosen using the criterion $\|\boldsymbol{F}_{rb}\| > \Gamma$.
3. Mass is exchanged between the fluid components at the evaporation sites using Eq. (14).

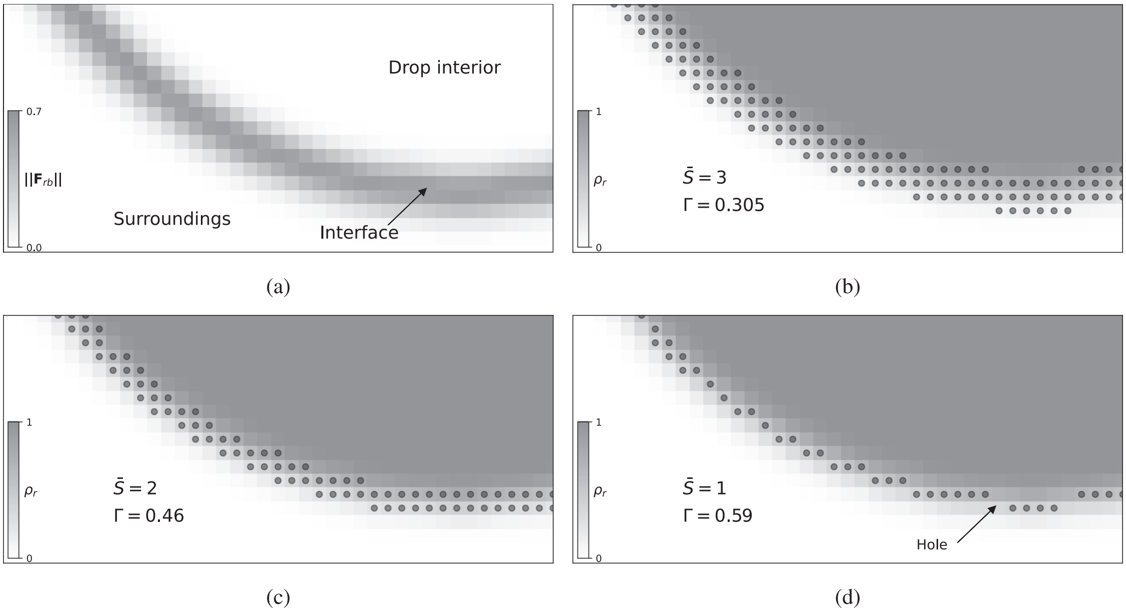

FIG. 1. (a) Color-gradient magnitude $\|\boldsymbol{F}_{rb}\|$ at different lattice sites for a spherical drop. (b)–(d) Evaporation sites (marked by •) selected at the spherical interface for different $\bar{S}$ and corresponding Γ (in lattice units). The colors show the density of the evaporating fluid ρ_r. The results shown are for the unit density ratio and $\beta = 0.99$.

4. The color-blind distribution $(f_i = \sum_k f_i^k)$ and macroscopic variables $(\rho_k = \sum_i f_i^k,\ \rho = \sum_k \rho_k$, and $\boldsymbol{u} = \frac{1}{\rho}\sum_i f_i \boldsymbol{c}_i)$ are determined.
5. Collision, perturbation, and recoloring operations are systematically carried out as per Eqs. (2), (5), and (7), respectively.
6. A streaming step is performed via Eq. (8), completing one timestep.

The color-gradient magnitude $\|\boldsymbol{F}_{rb}\|$ used in step 2 uses the value determined from the previous timestep during the perturbation step to save computational effort. It is evident that this procedure has a small computational overhead and does not change the core algorithm of the CG-LB method.

III. RESULTS AND DISCUSSION

We demonstrate RL evaporation using the method introduced in Sec. II B. During evaporation, we compare the interface positions in LB simulations with analytical solutions whenever possible. The simulations involve initializing a pair of fluid components (red-blue) and achieving equilibrium based on a domain-wide velocity-based convergence criterion of 10^{-7}. Subsequently, evaporation begins, with the red fluid assumed to be the evaporating component. The interface position is considered to be where the density of the evaporating fluid is half of the maximum value. No-slip boundary conditions are enforced on the walls using halfway-bounce back boundary conditions (BC).[56] Additionally, the walls are neutrally wetting. The units for quantities such as length, velocity, ρ, σ, τ, and ϕ and Γ are specified in their respective lattice units. The simulations are conducted with no density contrast $(\rho_r = \rho_b = 1)$, interface thickness parameter $\beta = 0.99$, surface tension $\sigma = 0.1$, and unit relaxation parameters $(\tau_r = \tau_b = 1)$, unless stated otherwise.

In Sec. III A, the effect of interface shape on the choice of Γ is shown for a given set of CG parameters and over a wide range of ϕ. Section III B investigates the effect of the CG model parameters on the choice of Γ. Section III C shows the accuracy of the current method in the case of space and time-varying evaporative flux. In Sec. III D, we discuss the findings and comment on the overall method. All results are shown henceforth with $\bar{S} = 3$.

A. Effect of interface shape

1. Flat interface

We consider a pseudo-one-dimensional domain with dimensions $[x, y, z] = 4 \times 128 \times 4$, where there are no-slip walls at the boundaries in the y-direction and periodic boundary conditions (BC) at the remaining boundaries. The simulation begins with red fluid up to $y = 80$ and the remaining space filled with blue fluid in the y-direction. For a constant mass flux ϕ leaving through surface area A_S and constant fluid density $\rho = \rho_0$, the height $h(t)$ of the interface as a function of time can be derived from Eq. (10) as

$$h(t) = h_0 - \frac{\phi}{\rho_0} t, \tag{16}$$

where h_0 represents the initial height of the interface. The time for complete evaporation can be calculated as $t_e = \frac{h_0 \rho_0}{\phi}$. Here, ρ_0 and h_0 correspond to the equilibrium values from the lattice Boltzmann (LB) simulation.

In Fig. 2(a), we compare LB and analytical results for the normalized height h/h_0 of the interface as a function of the normalized time $t^* = t/(h_0\rho_0/\phi)$. We find good agreement between the analytical and LB results for $\Gamma = 0.31$ for $\phi = 0.03, 0.003, 0.0003$, which

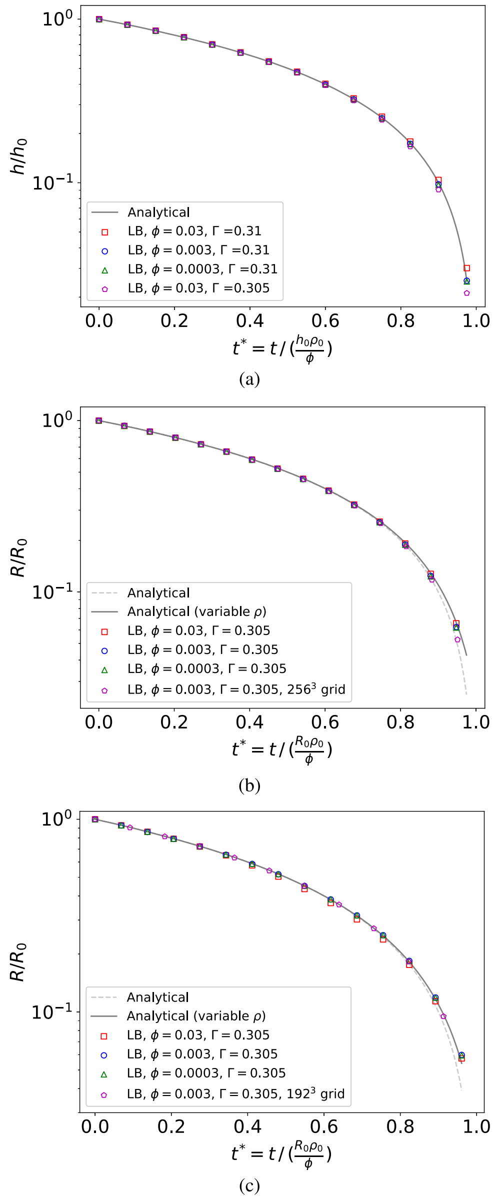

(a)

(b)

(c)

FIG. 2. Comparison between LB and analytical results for an evaporating (a) flat interface, (b) spherical drop, and (c) hemispherical drop. Plot of the normalized interface position (h/h_0 and R/R_0) with normalized time (t^*).

correspond to interface speeds of approximately $\frac{dh}{dt} \approx 0.03, 0.003, 0.0003$, respectively. The error between the LB simulation and analytical solution grows as the interface height becomes comparable to the interface thickness (≈ 5), especially at later stages of evaporation. Thus, we only report results up to $h/h_0 = 0.1$ at $t^* = 0.9$. We report the percentage error in the interface position (h/h_0) compared to the analytical solution. For $\phi = 0.0003$, the errors are found to be 0.33% and 2.7% at $t^* = 0.52$ and 0.9, respectively. Similarly, for $\phi = 0.03$, the errors are 0.4% at $t^* = 0.52$ and 3.9% at $t^* = 0.9$. These results suggest that the dependence of ϕ on the accuracy of the results is weak, indicating that a single value of Γ could be used regardless of the choice of ϕ.

Furthermore, we demonstrate the effect of Γ on the accuracy by including a result with $\Gamma = 0.305$ in Fig. 2(a). For $\phi = 0.03$ and $\Gamma = 0.305$, the errors are found to be 1.1% at $t^* = 0.52$ and 9.26% at $t^* = 0.9$. $\Gamma = 0.305$ will be used as a common threshold for comparison across all succeeding cases.

2. Freely suspended spherical drop

A three-dimensional (3D) domain of size 128^3 is used with periodic BC in all directions. The simulation is initialized with a sphere of red fluid of radius $R_0 = 44$ lattice nodes at the center of the domain and the surroundings with the blue fluid. For a constant mass flux ϕ leaving through surface area A_S and constant fluid density $\rho = \rho_0$, the radius $R(t)$ of the spherical interface as a function of time can be derived from Eq. (10) as

$$R(t) = R_0 - \frac{\phi}{\rho_0} t, \qquad (17)$$

where R_0 is the initial radius of the drop. The time to complete evaporation can be found as $t_e = \frac{R_0\rho_0}{\phi}$. ρ_0 and R_0 are taken as the equilibrium values from the LB simulation. Since pressure p and density ρ are related in LB via the equation of state [Eq. (4)], ρ depends on $R(t)$ because of the Laplace pressure. $R(t)$ can then be derived from Eq. (10), taking into account the variable density (shown in Appendix A), leading to

$$R(t) + \frac{4\sigma}{3c_s^2\rho_b} \ln\left(R(t)/R_0\right) = -\frac{\phi t}{\gamma\rho_b} + R_0. \qquad (18)$$

The above equation can be solved for $R(t)$ numerically.[57] We take the density of surrounding (blue) fluid $\rho_b = 1$, density ratio $\gamma = 1$, and lattice speed of sound $c_s = 1/\sqrt{3}$.

Figure 2(b) shows the comparison between the LB simulations and analytical results for the normalized drop radius R/R_0 vs the normalized time $t^* = t/(R_0\rho_0/\phi)$. For the analytical results, the effect of variable density is only visible at smaller radii ($R/R_0 < 0.1$) where the Laplace pressure becomes significant. We compare results till $t^* = 0.81$ ($R/R_0 = 0.18$) where the drop radius is still larger than the interface thickness. The error between the analytical and simulation results is $\approx 3\%$ at $t^* = 0.81$. Hence, the effect of variable density is insignificant. For $\Gamma = 0.305$, good agreement is found between the analytical (constant density) and LB results for $\phi = 0.03, 0.003, 0.0003$, which correspond to interface speeds of $\frac{dR}{dt} \approx 0.03, 0.003, 0.0003$, respectively. For $\phi = 0.0003$, the error is found to be 0.5% and 0.4% at $t^* = 0.54$ and 0.81, respectively. For $\phi = 0.03$, the error is found to be 0.2% and 2.1% at $t^* = 0.54$ and 0.81, respectively. Once again, for the chosen Γ, the results do not vary significantly with ϕ. A simulation performed on a 256^3 lattice using $R_0 = 88$ is also included in Fig. 2(b) to demonstrate that a single value of Γ leads to accurate results regardless of the drop size.

3. Hemispherical drop on substrate

Similar to Sec. III A 2, we use a 3D domain of size 128^3 with periodic boundaries with the exception of no-slip walls at the y-direction boundaries. The simulation is initialized with a hemisphere of red fluid of radius $R_0 = 44$ at the center of the bottom wall. Analytically, the radius $R(t)$ of the hemispherical drop evolves through Eqs. (17) and (18) for the constant and variable fluid density, respectively.

Figure 2(c) shows the comparison between LB and analytical results for normalized drop radius R/R_0 vs normalized time $t^* = t/(R_0\rho_0/\phi)$. Once again, we find the effect of variable density to be insignificant at $t^* = 0.81$, where we compare the results. For $\Gamma = 0.305$, good agreement is found between the analytical (constant density) and LB results for $\phi = 0.03, 0.003, 0.0003$, which correspond to interface speeds of $\frac{dR}{dt} \approx 0.03, 0.003, 0.0003$, respectively. For $\phi = 0.0003$, the error is found to be 0.23% and 4.28% at $t^* = 0.54$ and 0.81, respectively. For $\phi = 0.03$, the error is found to be 3.6% and 0.45% at $t^* = 0.54$ and 0.81, respectively. For faster evaporation rates ($\phi = 0.03$), the irregularity in error is observed due to the local contact angle deviating from 90^0 as the contact line moves. As a result, the drop deforms slightly out of its hemispherical shape. Data from a simulation on 192^3 lattice using $R_0 = 66$ are also included in Fig. 2(c) to demonstrate that the choice of Γ can be independent of the drop size.

4. Pinned spherical cap

A 3D domain of size 192^3 is used with no-slip walls at the y-direction boundaries and periodic BC at the remaining boundaries. A cylindrical cavity of inner radius 50, outer radius 53, and height 8 is placed at the center of the bottom wall. A spherical liquid drop is initialized such that its interface is pinned at the outer edge of the cavity at equilibrium, resulting in a contact angle of $\theta \approx 120^0$. The setup and equilibrium drop profile are shown in Figs. 3(a) and 3(b). For a constant mass flux ϕ leaving through surface area A_S and constant fluid density $\rho = \rho_0$, the height h of the spherical cap as a function of time can be derived from Eq. (10) as

$$h(t) = h_0 - \frac{2\phi}{\rho_0} t, \tag{19}$$

where h_0 is the initial height of the spherical cap. The time to complete evaporation can be found as $t_e = \frac{h_0\rho_0}{2\phi}$. ρ_0 and h_0 (excluding the cavity height) are taken as the equilibrium values from the LB simulation. $h(t)$ can also be derived from Eq. (10), taking into account the variable density (shown in Appendix B), leading to

$$\begin{aligned} h(t) + \frac{4\sigma}{3c_s^2\rho_b}\left[\ln\left(\frac{a^2 + h(t)^2}{a^2 + h_0^2}\right) - \frac{a^4}{(a^2 + h(t)^2)^2}\right] \\ = \frac{-2\phi t}{\gamma\rho_b} + h_0 - \frac{4\sigma}{3c_s^2\rho_b}\frac{a^4}{(a^2 + h_0^2)^2}, \end{aligned} \tag{20}$$

where a is the drop contact radius (constant) taken equal to the equilibrium value from the LB simulation ($a = a_0$). We take the density of the surrounding (blue) fluid $\rho_b = 1$, the density ratio $\gamma = 1$, and the lattice speed of sound $c_s = 1/\sqrt{3}$. Equation (20) is solved for $h(t)$ numerically.[57]

The contact radius is determined by tracking the interface position in a plane just above the cylindrical cavity. As shown in Fig. 3(c), the contact line moves slowly instead of becoming immobilized. A similar behavior has been observed when pinning the contact line with wetting boundary conditions.[58] For the current case, unpinning happens when the contact line reaches the inner edge of the cylindrical cavity ($a/a_0 = 0.95$) and, subsequently, starts to move downward

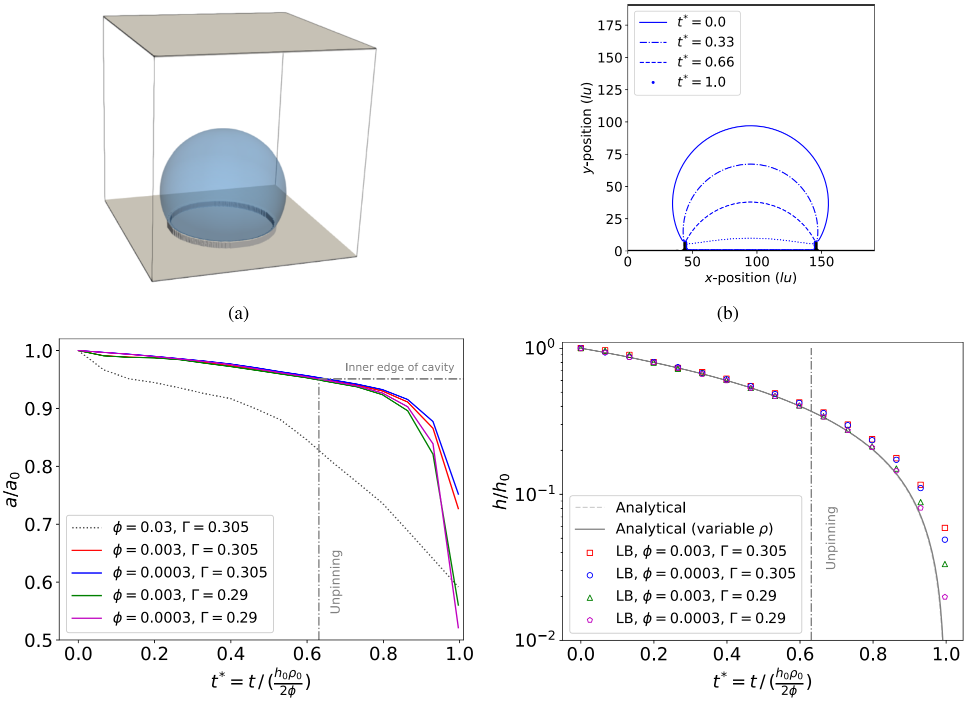

(a) (b)

(c) (d)

FIG. 3. (a) 3D view of pinned spherical drop resting on top of the cylindrical cavity, with walls on the top and bottom of the domain. (b) Drop profile at various stages of evaporation, slice taken at z-position midpoint. (c) Plot of the normalized LB contact radius (a/a_0) with normalized time (t^*). (d) Comparison between LB and analytical results. Plot of the normalized drop height h/h_0 with normalized time (t^*).

[shown in Fig. 3(b)]. $\phi = 0.03$ has not been considered in the results as it leads to a premature unpinning of the contact line, as shown by the dotted line in Fig. 3(c).

Figure 3(d) shows the comparison between LB and analytical results for the normalized drop height h/h_0 vs normalized time $t^* = t/(h_0\rho_0/2\phi)$. Results are compared till unpinning, which for most cases occurs near $t^* \approx 0.63$ [Fig. 3(c)]. For analytical solutions, the difference between the constant and variable density results is insignificant owing to the lack of high curvatures. For $\Gamma = 0.305$ (the threshold used in previous sections), the error between the LB simulation and the analytical solution at the nearest data point after unpinning (at $t^* = 0.664$) is found to be 8% and 7% for $\phi = 0.003$ and 0.0003, respectively, while at $t^* = 0.332$, the error is 2.5% and 1.2% for $\phi = 0.003$ and 0.0003, respectively. It should be noted that the analytical solution assumes the contact radius to be fixed throughout the evaporation, while the same drifts in the simulations [shown in Fig. 3(c)]; hence, some error is expected. The same can be offset by adjusting the threshold. For $\Gamma = 0.29$, good agreement is found between the analytical and LB results for $\phi = 0.003$ and 0.0003 with errors of 1.9% and 0.7% at unpinning, respectively.

B. Effect of parameters of the color-gradient model

1. Interface thickness parameter

The interface thickness in the CG-LB method is determined by the parameter β, which ranges from 0 to 1. Here, we present results for β values of 0.99, 0.9, 0.8, and 0.7, corresponding to interface thicknesses of ~5, 6, 7 and 8 lattice nodes, respectively. The benchmarks for flat and spherical interfaces in Secs. III A 1 and III A 2 are repeated with varying β in Figs. 4(a) and 4(b), respectively. It can be observed that parameter Γ varies weakly with the interface thickness. A maximum difference (absolute) of 0.005 is observed in Γ across all the β values considered for each of the flat and spherical cases. Additionally, the difference in Γ between the flat and spherical cases remains consistent for a given β ($|\Gamma_{flat} - \Gamma_{sphere}| = 0.005$). Thus, changing the interface thickness has a minor effect on Γ, and this effect is uniform across different interface shapes. It is also evident that changing the interface thickness does not affect the accuracy of the method, as shown in Fig. 4, where the results for all β show similar deviations from the analytical results. We conclude that the interface thickness should be considered when selecting Γ, but the method itself is not constrained by the interface thickness beyond standard numerical resolution considerations.

2. Density contrast

In the case of a density contrast ($\gamma \neq 1$), an outlet for the non-evaporating fluid component (blue fluid) needs to be added in the domain to maintain the desired density ratio between the two components. This was not necessary for the unit density ratio cases shown previously. We use a pressure boundary condition[59,60] to implement the outlet for the blue fluid. We replicate the benchmark from Sec. III A 2 for a spherical interface with a drop radius $R_0 = 44$ and a domain size of 192^3. The simulation is initiated with $\rho_r = 2$, $\rho_b = 1$ for $\gamma = 2$ and $\rho_r = 4$, $\rho_b = 1$ for $\gamma = 4$, followed by equilibration. During the evaporation stage, outlets are specified at each of the z-direction boundaries for the blue fluid with $\rho_b = 1$ enforced.

Figure 5(a) compares LB and analytical (constant density) results for a spherical interface with $\gamma = 2$ and 4. The following range of errors are reported in the interval $t^* = 0.5$–0.85. For $\gamma = 2$ and $\Gamma = 0.32$, the error is found to be 2.6%–8.7% and 0.17%–1.1% for $\phi = 0.03$ and 0.003, respectively. For $\gamma = 4$ and $\Gamma = 0.33$, the error is found to be 5.7%–17.1% and 2%–4.6% for $\phi = 0.03$ and 0.003, respectively. In both cases, good agreement is found for smaller ϕ, while the error increases for larger ϕ and higher γ.

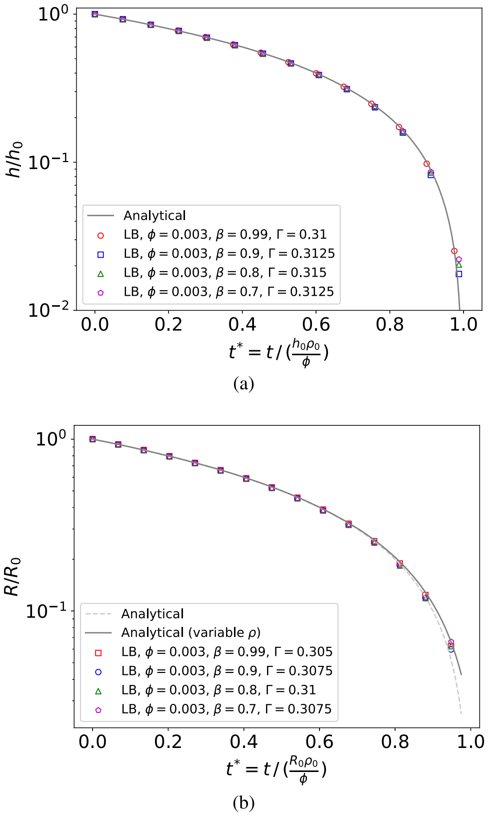

(a)

(b)

FIG. 4. Comparison between LB simulations and analytical results for an evaporating (a) flat interface and (b) a spherical drop for varying β. Plot of the normalized interface position (h/h_0 and R/R_0) with normalized time (t^*).

This behavior differs from the observations for $\gamma = 1$, where the accuracy was weakly dependent on ϕ. This difference stems from the outlet boundary conditions used for the density contrast cases. For smaller ϕ, the outlet boundary conditions can maintain the blue fluid at the desired density. However, for larger ϕ, the blue fluid may accumulate over the interface, leading to an increase in density (ρ_b), which then affects the magnitude of the color-gradient and the accuracy of the results. Depending on the domain geometry and the location/number of outlets, the accuracy can vary significantly when using larger ϕ.

Figure 5(b) recreates the flat interface benchmark from Sec. III A 1 for $\gamma = 2$ and 4, with an increased domain size of 160^3 lattice nodes and an outlet at the upper y-direction boundary. For the case of $\phi = 0.03$ and $\gamma = 4$, we observe the effect described in the previous paragraph more prominently than in the spherical case. The error in the interface position h/h_0 increases significantly, deviating

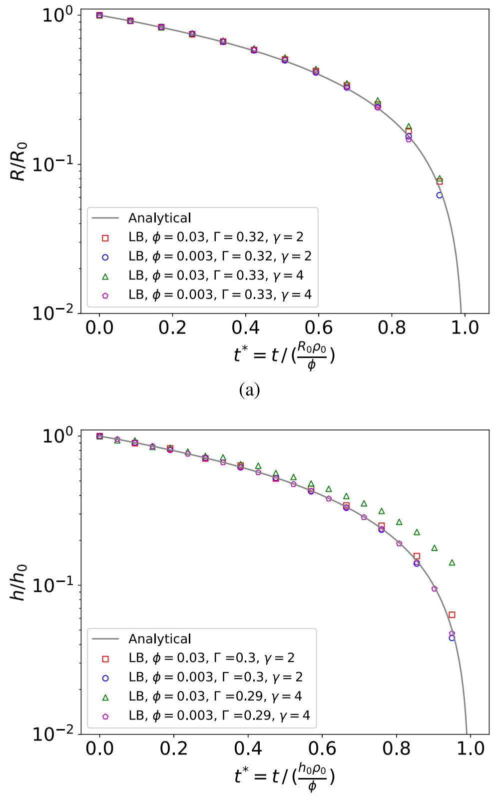

(a)

(b)

FIG. 5. Comp arison between LB simulations and analytical results for an evaporating (a) spherical drop and (b) a flat interface for density ratio $\gamma = 2$ and 4. Plot of the normalized interface position (h/h_0 and R/R_0) with normalized time (t^*).

away from the analytical solution as the evaporation proceeds. Nevertheless, as shown in Fig. 5(b), accurate results can still be achieved with smaller ϕ and γ.

It is observed that as γ increases, the difference in threshold Γ between the flat and spherical interfaces also increases: $|\Gamma_{flat} - \Gamma_{sphere}| = 0.02$ and 0.04 for $\gamma = 2$ and 4, respectively. It suggests that Γ must be chosen separately for different shapes of the interface to get accurate results for $\gamma > 1$. In contrast, for $\gamma = 1$, as shown in Sec. III A, a single value of Γ gives fairly accurate results across different interface shapes. Hence, the threshold Γ needs to be fine-tuned to suit applications involving density contrast and different interface shapes.

C. Evaporation with space and time-varying flux

Unlike the results shown in Secs. III A and III B, we now assume a space and time varying evaporative flux. Based on theoretical works of drops evaporating on heated substrates in the reaction-limited regime,[3,8,18] we adopt a commonly used expression for the flux Φ^* (dimensionless) at the interface, neglecting the Laplace correction and the substrate thickness. It is given by

$$\Phi^* = \frac{1}{K + h^*}, \tag{21}$$

TABLE I. Reported error in the interface position for an evaporating hemispherical drop with variable flux Φ for different K, with $\Gamma = 0.305$.

K	$\Phi_{\max}/\Phi_{\min}$	Error (%)	At R/R_0
1	2	6.71	0.23
0.5	3	14.39	0.21
0.25	5	43.83	0.2

where h^* is the local height of the drop (dimensionless) and K is a constant related to the kinetic effects and volatility of the liquid.[8] Φ^* varies with drop height as such that the flux is higher near the contact line ($h^* \to 0$) as compared to the top of the drop ($h^* \to 1$).

We recreate the benchmark from Sec. III A 3 for a hemispherical drop on a 192^3 domain and with $R_0 = 66$ using Φ^*. The schematic for the problem depicting relevant parameters is shown in Fig. 6(a). The initial drop radius R_0 is taken as the length scale, ϕ_S is taken as the flux scale, and R_0^2/ν is taken as the viscous time scale. The dimensional flux can be written as $\Phi = \phi_S\, \Phi^*$ and $h^* = h/R_0$. For constant density (assumed for simplicity) and flux Φ, Eq. (10) can be solved (shown in Appendix C) to recover the following differential equation for the drop radius $R(t)$:

$$\frac{dR(t)}{dt} = \frac{\phi_S\, R_0}{\rho\, R(t)} \ln\left(\frac{KR_0}{R(t) + KR_0}\right). \tag{22}$$

Equation (22) is solved numerically[57] with the initial condition $R(t = 0) = R_0$.

For $K = 1, 0.5$, and 0.25, the variation of Φ^* with the normalized radial coordinate r/R is shown in Fig. 6(b). Initially ($R/R_0 = 1$), Φ^* increases toward the contact line ($r/R \to 1$) with the maximum increase for $K = 0.25$ and a minimum increase for $K = 1$. Near the end of the evaporation ($R/R_0 = 0.1$), the variation of flux across the interface diminishes for all K as a smaller height of the drop remains. Hence, Φ^* varies both with space and time. The mass flux scale ϕ_S is kept fixed at 0.001. The dimensional flux Φ can then be converted to a mass sink rate φ for LB simulations using Eq. (13) at different evaporation sites depending upon the local height h^*.

Figure 6(c) shows the comparison between LB and analytical results for the normalized drop radius R/R_0 vs the normalized time $t^* = t/(R_0^2/\nu)$ with variable flux Φ using $K = 1$, 0.5, and 2.5. The results presented use the same $\Gamma = 0.305$ as in Sec. III A 3. We report the error at the closest data point to $R/R_0 \approx 0.2$ (Table I). The agreement between LB and analytical results is better for larger K, i.e., smaller differences between the maximum and minimum values of flux ($\Phi_{\max}/\Phi_{\min}$). For $K = 0.5$, an error of $\approx$14% is observed corresponding to $\Phi_{\max}/\Phi_{\min} = 3$, which marks the limit of the current method. For $K > 1$, the flux does not vary strongly with space and time ($\Phi_{\max}/\Phi_{\min} \approx 1$), and the error is expected to be much lower (not shown here). Therefore, the current method can be used with weakly space-time varying flux with reasonable error. It is to be noted that with a larger evaporation rate close to the contact line, the drop can slightly deform out of the hemispherical shape, leading to some error in the early stages of evaporation [visible for $K = 0.25$ in Fig. 6(c)].

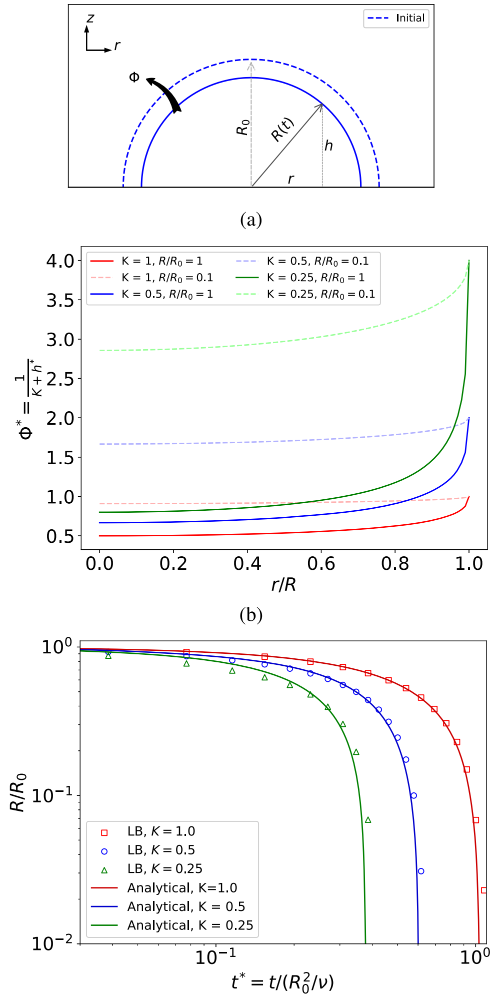

(a)

(b)

(c)

FIG. 6. (a) Schematic of hemispherical drop evaporating from a substrate with space and time varying flux Φ at the interface. (b) Variation of evaporative flux Φ^* with radial positions r/R for different K at the beginning ($R/R_0 = 1$) and nearing the end ($R/R_0 = 0.1$) of evaporation. (c) Comparison between LB and analytical results for variable flux Φ at different K. Plot of the normalized drop radius (R/R_0) with normalized time (t^*).

TABLE II. Reported error in the interface position for cases considered in Sec. III A for $\Gamma = 0.305$.

Interface shape		Error in interface position (%)[a]
Flat	Section III A 1	1.1–9.26
Spherical	Section III A 2	0.2–2.1
Hemispherical	Section III A 3	0.45–3.6
Pinned spherical cap	Section III A 4	2.5–8

[a] Reported at the largest ϕ wherever possible.

D. Method overview

We summarize the findings from Secs. III A–III C and comment on the optimum strategy for choosing Γ. Table II shows the error in the interface position for different shapes considered in Sec. III A when a common $\Gamma = 0.305$ is used and for the largest ϕ possible. A maximum error of ∼9% is observed for the flat interface, while it is under 8% for the curved interfaces. The upper range of the error is generally observed at the end of evaporation and is not indicative of the majority duration, for which the error is usually well under 5%. The interface shapes considered to span from no curvature (flat) to increasing curvature (spherical and hemispherical) to decreasing curvature (pinned spherical cap). Different drop evaporation modes, namely, constant contact angle and constant contact radius, are also taken into account in the hemispherical and pinned spherical cap cases. Therefore, a single value of Γ could be used for a general shape of the interface with reasonable error for the unit density ratio and associated set of CG model parameters. The optimum value of Γ could be obtained by recreating some of the benchmarks detailed in Sec. III A for flat and curved interfaces. If the shape of the interface and its evolution are previously known, then Γ could be adjusted for better accuracy via comparison with analytical or numerical results. In practical applications with dynamically evolving interfaces, some errors may accumulate over time as the interface shape continuously changes. These errors may be offset via dynamically adjusting the evaporation flux ϕ as needed.

From the results in Sec. III B, Γ is found to be mainly dependent on the interface thickness and density ratio. However, the effect of changing the interface thickness on Γ was observed to be uniform across different shapes, thus maintaining generality. For $\gamma = 1$, the method is shown to work reliably over a wide range of evaporative flux and interface shapes. For $\gamma \neq 1$, the method requires an outlet for the non-evaporating fluid component to maintain the desired density ratio. Accurate results are observed when both ϕ and γ are kept small. Additionally, it is recommended to tune Γ on a case-by-case basis for accurate results.

While the current model for RL evaporation is derived for a constant flux ϕ (Sec. II B), the results from Sec. III C demonstrate that it can be used with space and time-varying flux as long as the variation in the flux is not large ($\Phi_{\max}/\Phi_{\min} \leq 3$). For constant flux and unit density ratio, the method has shown good accuracy over two orders of magnitude of evaporative flux ($\phi = 0.01$–0.0001), covering both the fast and slow evaporation rates. The maximum rate is limited by the fluid density of the evaporating fluid component (ρ_r) and the fluid interface speed being less than 0.1 (to avoid compressibility errors).

The dependence of Γ on $\bar{S}$ was shown in Figs. 1(b), 1(c), and 1(d). $\bar{S} > 1$ is recommended to avoid holes in the selected evaporation sites around the interface. Additionally, $\bar{S} = 3$ was used in the current study due to the minimal dependence of ϕ on the accuracy of the results for a given Γ. The same dependence was found to increase for $\bar{S} < 3$. For instance, between $\phi = 0.03$ and 0.003, the error is found to vary by ∼1.5%, 9.5%, and 13% for $\bar{S} = 3$, 2, and 1, respectively, for the spherical interface case (Sec. III A 2).

IV. CONCLUSION

We have developed a method for achieving reaction-limited evaporation for the CG LB multicomponent model and have successfully validated it against analytical solutions for various interface shapes. This method involves tuning a single free parameter (threshold) to select evaporation sites at the interface and then exchanging the fluid mass between the components. We have demonstrated that a single threshold value can be used for a general shape of the interface with reasonable error over a wide range of flux magnitudes for a given set of CG model parameters, especially for the unit density ratio. However, for density contrast, we recommend using smaller evaporation fluxes and density ratios for accurate results.

Our method utilizes the inherently calculated color-gradient magnitude and the resting populations for mass exchange, making it computationally inexpensive, locally applicable, and easy to implement. Importantly, it does not require any changes to the core algorithm of CG, making it compatible with other CG variants as well. Similar to the NEOS models used in theoretical studies, evaporation occurs solely at the interface and is decoupled from the vapor phase dynamics. In principle, the same approach could be extended to other multicomponent LB models (pseudo-potential and free-energy) using the color-gradient magnitude to identify the evaporation sites followed by a mass exchange between the components. However, investigating the stability of the interface due to the mass exchange is necessary to achieve consistent results. In CG, the robustness of the recoloring step led to stable and accurate results.

The current method with constant evaporation flux can be used to study isothermal RL evaporation, for example, when there is a neutral gas draft over the interface. The flux can be modeled by the Hertz–Knudsen relation as done by Hernandez-Perez *et al.*[61] for the evaporation of drops from millimeter-sized pillars, showing good agreement with experimental results. The current method can also be used to study non-isothermal RL evaporation if the flux varies weakly with space and time. For drop evaporation on heated substrates, the experimental value for the K parameter in the space-time varying flux [Eq. (21) used in Sec. III C] is $K = 10$ for water and $K = 1$ for isopropanol as suggested by Murisic and Kondic.[3] As a result, the flux varies weakly with the drop height for these fluids, and the current method can be used with reasonable error for such applications. The method also extends the CG model to study evaporation in porous media with possible applications in soil water evaporation[12] and polymer electrolyte fuel cells.[13]

ACKNOWLEDGMENTS

We thank Marcello Sega and Johannes Hielscher for fruitful discussions and technical support. We gratefully acknowledge the financial support provided by the Deutsche Forschungsgemeinschaft (DFG) through the research unit FOR2688 "Instabilities, Bifurcations and Migration in Pulsatile Flows" (Project No. 349558021) and the collaborative research centers SFB1411 (Project No. 416229255) and SFB1452 (Project No. 431791331).

AUTHOR DECLARATIONS

Conflict of Interest

The authors have no conflicts to disclose.

Author Contributions

Gaurav Nath: Conceptualization (equal); Data curation (equal); Formal analysis (equal); Software (equal); Validation (equal); Visualization (equal); Writing – original draft (equal). **Othmane Aouane**: Conceptualization (equal); Validation (equal); Writing – review & editing (equal). **Jens Harting**: Conceptualization (equal); Funding acquisition (equal); Writing – review & editing (equal).

DATA AVAILABILITY

The data that support the findings of this study are openly available in Zenodo at http://doi.org/10.5281/zenodo.13382917.

APPENDIX A: $R(t)$ FOR A SPHERICAL DROP WITH VARIABLE DENSITY

For a pair of fluid components (ρ_r, ρ_b) with density ratio $\gamma = \rho_r/\rho_b$ ($\rho_r > \rho_b$) and surface tension σ, the pressure p in each component is given by [using Eq. (4)]

$$p_b = \rho_b \zeta [1 - W_0] = \rho_b \, c_s^2, \tag{A1}$$

$$p_r = \rho_r \zeta \frac{[1 - W_0]}{\gamma} = \frac{\rho_r \, c_s^2}{\gamma}. \tag{A2}$$

Assuming red fluid inside the spherical drop and blue fluid surrounding it, according to the Young–Laplace equation, we have

$$p_r - p_b = \frac{2\sigma}{R}. \tag{A3}$$

Substituting the pressures from Eqs. (A1) and (A2) in the above expression, we get

$$\rho_r = \gamma \left[\rho_b + \frac{2\sigma}{R c_s^2} \right]. \tag{A4}$$

Here, we assume ρ_b to be a constant. For a constant mass flux ϕ leaving through surface area A_S and variable density $\rho(t)$, Eq. (10) can be written as

$$\frac{d(\rho V)}{dt} = -\phi A_S, \tag{A5}$$

$$\frac{dV}{dt} = -\frac{\phi}{\rho} A_S - \frac{V}{\rho} \frac{d\rho}{dt}. \tag{A6}$$

Substituting volume $V = (4/3)\pi R^3$, surface area $A_S = 4\pi R^2$, and Eq. (A4) for ρ in the above equation leads to

$$\frac{dR}{dt} = -\frac{\phi/\gamma}{\frac{4\sigma}{3Rc_s^2} + \rho_b}. \tag{A7}$$

Solving the above differential equation using the initial condition $R = R_0$ at $t = 0$, we get

$$R(t) + \frac{4\sigma}{3c_s^2 \rho_b} \ln\left(R(t)/R_0\right) = -\frac{\phi t}{\gamma \rho_b} + R_0. \tag{A8}$$

This equation is solved for $R(t)$ numerically.[57]

APPENDIX B: $h(t)$ FOR A PINNED SPHERICAL DROP WITH VARIABLE DENSITY

For a spherical cap with contact radius a and height h, volume V and surface area A_S of the spherical cap are given by $V = \frac{1}{6}\pi h(3a^2 + h^2)$ and $A = \pi(a^2 + h^2)$, respectively. The density of the drop ρ is given by Eq. (A4), where $R = \frac{a^2+h^2}{2h}$ is the radius of curvature of the spherical cap. Substituting volume V, surface area A_S, and ρ in Eq. (A6) and simplifying for $h(t)$, we get

$$\frac{dh}{dt} = \frac{-2\phi/\gamma}{\frac{4\sigma h}{(a^2+h^2)c_s^2} + \rho_b + \frac{4\sigma}{3c_s^2}\, h\,(3a^2+h^2)\,\frac{a^2-h^2}{(a^2+h^2)^3}}, \tag{B1}$$

where the contact radius a is taken as constant for the pinned spherical cap. Solving the above differential equation using the initial condition $h = h_0$ at $t = 0$, we get

$$h(t) + \frac{4\sigma}{3c_s^2\rho_b}\left[\ln\left(\frac{a^2 + h(t)^2}{a^2 + h_0^2}\right) - \frac{a^4}{(a^2 + h(t)^2)^2}\right] = \frac{-2\phi t}{\gamma\rho_b} + h_0 - \frac{4\sigma}{3c_s^2\rho_b}\,\frac{a^4}{(a^2 + h_0^2)^2}. \tag{B2}$$

The above equation is solved for $h(t)$ numerically.[57]

APPENDIX C: $R(t)$ FOR A HEMISPHERICAL DROP WITH SPACE AND TIME VARYING FLUX

We choose cylindrical coordinates (r, θ, z) for the current case with the problem schematic and relevant parameters shown in Fig. 6(a). The initial drop radius $R(t = 0) = R_0$ is chosen as the length scale. For a hemispherical drop, the drop height at any given r is given by $h = \sqrt{R(t)^2 - r^2}$ and the normalized height is given by $h^* = h/R_0$.

Let Φ^* be the space- and time-varying flux (non-dimensional) at the interface dependent on the local drop height h^*, as given by

$$\Phi^* = (K + h^*)^{-1} = \left(K + \frac{\sqrt{R(t)^2 - r^2}}{R_0}\right)^{-1}, \tag{C1}$$

where K is a constant. Φ^* can be written in a dimensional form assuming a flux scale ϕ such that $\Phi = \phi_S\,\Phi^*$.

Equation (10) for constant ρ and variable flux $\Phi = \phi_S\,\Phi^*$ can be written as

$$\frac{dV}{dt} = \frac{-\phi_S}{\rho}\iint_{A_S}\Phi^*\, dA_S. \tag{C2}$$

In cylindrical coordinates, the elemental surface area on the hemisphere is given by

$$dA_S = \frac{R}{\sqrt{R^2 - r^2}}\, r\, dr\, d\theta. \tag{C3}$$

Substituting dA_S from the above equation, $V = \frac{2}{3}\pi R^3$, and Φ^* from Eq. (C1) in Eq. (C2), we get

$$\frac{d}{dt}\left(\frac{2}{3}\pi R^3\right) = -\frac{\phi_S}{\rho}\int_0^{2\pi}\int_0^R\left(K + \frac{\sqrt{R(t)^2 - r^2}}{R_0}\right)^{-1} \times \frac{R}{\sqrt{R^2 - r^2}}\, r\, dr\, d\theta. \tag{C4}$$

After simplifying, we then get

$$\frac{dR(t)}{dt} = \frac{\phi_S\, R_0}{\rho\, R(t)}\ln\left(\frac{KR_0}{R(t) + KR_0}\right). \tag{C5}$$

The above differential equation is solved for $R(t)$ numerically via an explicit Runge–Kutta method[57] of order 5(4) with the initial condition $R(t = 0) = R_0$.

REFERENCES

[1] H. Hu and R. G. Larson, "Analysis of the microfluid flow in an evaporating sessile droplet," Langmuir **21**, 3963–3971 (2005).

[2] G. J. Dunn, S. K. Wilson, B. R. Duffy, S. David, and K. Sefiane, "A mathematical model for the evaporation of a thin sessile liquid droplet: Comparison between experiment and theory," Colloids Surf., A **323**, 50–55 (2008).

[3] N. Murisic and L. Kondic, "On evaporation of sessile drops with moving contact lines," J. Fluid Mech. **679**, 219–246 (2011).

[4] J. M. Stauber, S. K. Wilson, B. R. Duffy, and K. Sefiane, "On the lifetimes of evaporating droplets," J. Fluid Mech. **744**, R2 (2014).

[5] P. J. Sáenz, A. W. Wray, Z. Che, O. K. Matar, P. Valluri, J. Kim, and K. Sefiane, "Dynamics and universal scaling law in geometrically-controlled sessile drop evaporation," Nat. Commun. **8**, 14783 (2017).

[6] T. A. Nguyen, S. R. Biggs, and A. V. Nguyen, "Analytical model for diffusive evaporation of sessile droplets coupled with interfacial cooling effect," Langmuir **34**, 6955–6962 (2018).

[7] H. Masoud, P. D. Howell, and H. A. Stone, "Evaporation of multiple droplets," J. Fluid Mech. **927**, R4 (2021).

[8] C. Larsson and S. Kumar, "Comparison of one-sided and diffusion-limited evaporation models for thin liquid droplets," J. Fluid Mech. **976**, A25 (2023).

[9] A.-M. Cazabat and G. Guéna, "Evaporation of macroscopic sessile droplets," Soft Matter **6**, 2591–2612 (2010).

[10] S. Whitaker, "Simultaneous heat, mass, and momentum transfer in porous media: A theory of drying," Adv. Heat Transfer **13**, 119–203 (1977).

[11] F. Ahmad, M. Talbi, M. Prat, E. Tsotsas, and A. Kharaghani, "Non-local equilibrium continuum modeling of partially saturated drying porous media: Comparison with pore network simulations," Chem. Eng. Sci. **228**, 115957 (2020).

[12] Z. Li, J. Vanderborght, and K. M. Smits, "Evaluation of model concepts to describe water transport in shallow subsurface soil and across the soil–air interface," Transp. Porous Media **128**, 945–976 (2019).

[13] M. A. Safi, N. I. Prasianakis, J. Mantzaras, A. Lamibrac, and F. N. Büchi, "Experimental and pore-level numerical investigation of water evaporation in gas diffusion layers of polymer electrolyte fuel cells," Int. J. Heat Mass Transfer **115**, 238–249 (2017).

[14] J. Chu, Y. Bao, X. Li, M. Wang, and F. Gao, "Kinetic study of Mn vacuum evaporation from Mn steel melts," Sep. Purif. Technol. **255**, 117698 (2021).

[15] T. Poullain, J.-P. Bellot, J. Jourdan, I. Crassous, and A. Jardy, "Vacuum evaporation and expansion of pure metals at high temperature: Application to titanium and zirconium," Vacuum **203**, 111209 (2022).

[16] S. Semenov, V. M. Starov, R. G. Rubio, and M. G. Velarde, "Computer simulations of evaporation of pinned sessile droplets: Influence of kinetic effects," Langmuir **28**, 15203–15211 (2012).

[17] K. L. Maki and S. Kumar, "Fast evaporation of spreading droplets of colloidal suspensions," Langmuir **27**, 11347–11363 (2011).

[18] T. Pham and S. Kumar, "Drying of droplets of colloidal suspensions on rough substrates," Langmuir **33**, 10061–10076 (2017).

[19] H. Hertz, "Ueber die verdunstung der flüssigkeiten, insbesondere des quecksilbers, im luftleeren raume," Ann. Phys. **253**, 177–193 (1882).

[20] M. Knudsen, "Die maximale verdampfungsgeschwindigkeit des quecksilbers," Ann. Phys. **352**, 697–708 (1915).

[21] A. H. Persad and C. A. Ward, "Expressions for the evaporation and condensation coefficients in the Hertz-Knudsen relation," Chem. Rev. **116**, 7727–7767 (2016).

[22] V. S. Ajaev, "Spreading of thin volatile liquid droplets on uniformly heated surfaces," J. Fluid Mech. **528**, 279–296 (2005).

[23] C. Sodtke, V. S. Ajaev, and P. Stephan, "Dynamics of volatile liquid droplets on heated surfaces: Theory versus experiment," J. Fluid Mech. **610**, 343–362 (2008).

[24] N. Murisic and L. Kondic, "Modeling evaporation of sessile drops with moving contact lines," Phys. Rev. E **78**, 065301 (2008).

[25] H. Liu, Q. Kang, C. R. Leonardi, S. Schmieschek, A. Narváez, B. D. Jones, J. R. Williams, A. J. Valocchi, and J. Harting, "Multiphase lattice Boltzmann simulations for porous media applications: A review," Comput. Geosci. **20**, 777–805 (2016).

[26] A. K. Gunstensen, D. H. Rothman, S. Zaleski, and G. Zanetti, "Lattice Boltzmann model of immiscible fluids," Phys. Rev. A **43**, 4320 (1991).

[27] A. K. Gunstensen and D. H. Rothman, "Microscopic modeling of immiscible fluids in three dimensions by a lattice Boltzmann method," Europhys. Lett. **18**, 157 (1992).

[28] J. Zhao, F. Qin, D. Derome, and J. Carmeliet, "Simulation of quasi-static drainage displacement in porous media on pore-scale: Coupling lattice Boltzmann method and pore network model," J. Hydrol. **588**, 125080 (2020).

[29] Z. Diao, S. Li, W. Liu, H. Liu, and Q. Xia, "Numerical study of the effect of tortuosity and mixed wettability on spontaneous imbibition in heterogeneous porous media," Capillarity **4**, 50–62 (2021).

[30] W. Lin, S. Xiong, Y. Liu, Y. He, S. Chu, and S. Liu, "Spontaneous imbibition in tight porous media with different wettability: Pore-scale simulation," Phys. Fluids **33**, 032013 (2021).

[31] X. Fu, Y. Ba, and J. Sun, "Numerical study of thermocapillary migration behaviors of droplets on a grooved surface with a three-dimensional color-gradient lattice Boltzmann model," Phys. Fluids **33**, 062108 (2021).

[32] X. Fu, J. Sun, and Y. Ba, "Numerical study of droplet thermocapillary migration behavior on wettability-confined tracks using a three-dimensional color-gradient lattice Boltzmann model," Phys. Fluids **34**, 012119 (2022).

[33] X. Fu and J. Sun, "Three-dimensional color-gradient lattice Boltzmann model for simulating droplet ringlike migration under an omnidirectional thermal gradient," Int. J. Therm. Sci. **184**, 107972 (2023).

[34] A. Montessori, M. Lauricella, N. Tirelli, and S. Succi, "Mesoscale modelling of near-contact interactions for complex flowing interfaces," J. Fluid Mech. **872**, 327–347 (2019).

[35] A. Montessori, M. Lauricella, A. Tiribocchi, and S. Succi, "Modeling pattern formation in soft flowing crystals," Phys. Rev. Fluids **4**, 072201 (2019).

[36] S. Leclaire, A. Parmigiani, O. Malaspinas, B. Chopard, and J. Latt, "Generalized three-dimensional lattice Boltzmann color-gradient method for immiscible two-phase pore-scale imbibition and drainage in porous media," Phys. Rev. E **95**, 033306 (2017).

[37] Z. Wen, Q. Li, Y. Yu, and K. H. Luo, "Improved three-dimensional color-gradient lattice Boltzmann model for immiscible two-phase flows," Phys. Rev. E **100**, 023301 (2019).

[38] T. Lafarge, P. Boivin, N. Odier, and B. Cuenot, "Improved color-gradient method for lattice Boltzmann modeling of two-phase flows," Phys. Fluids **33**, 082110 (2021).

[39] A. Subhedar, "Color-gradient lattice Boltzmann model for immiscible fluids with density contrast," Phys. Rev. E **106**, 045308 (2022).

[40] P. Mora, G. Morra, and D. A. Yuen, "Optimal surface-tension isotropy in the Rothman-Keller color-gradient lattice Boltzmann method for multiphase flow," Phys. Rev. E **103**, 033302 (2021).

[41] X. Shan and H. Chen, "Lattice Boltzmann model for simulating flows with multiple phases and components," Phys. Rev. E **47**, 1815 (1993).

[42] M. R. Swift, E. Orlandini, W. Osborn, and J. Yeomans, "Lattice Boltzmann simulations of liquid-gas and binary fluid systems," Phys. Rev. E **54**, 5041 (1996).

[43] D. Hessling, Q. Xie, and J. Harting, "Diffusion dominated evaporation in multicomponent lattice Boltzmann simulations," J. Chem. Phys. **146**, 054111 (2017).

[44] R. Ledesma-Aguilar, D. Vella, and J. M. Yeomans, "Lattice-Boltzmann simulations of droplet evaporation," Soft Matter **10**, 8267–8275 (2014).

[45] Q. Xie and J. Harting, "From dot to ring: The role of friction in the deposition pattern of a drying colloidal suspension droplet," Langmuir **34**, 5303–5311 (2018).

[46] Q. Xie and J. Harting, "The effect of the liquid layer thickness on the dissolution of immersed surface droplets," Soft Matter **15**, 6461–6468 (2019).

[47] L. Fei, F. Qin, J. Zhao, D. Derome, and J. Carmeliet, "Pore-scale study on convective drying of porous media," Langmuir **38**, 6023–6035 (2022).

[48] L. Fei, D. Derome, and J. Carmeliet, "Pore-scale study on the effect of heterogeneity on evaporation in porous media," J. Fluid Mech. **983**, A6 (2024).

[49] M. Zhao and X. Yong, "Modeling evaporation and particle assembly in colloidal droplets," Langmuir **33**, 5734–5744 (2017).

[50] M. Zhao, W. Luo, and X. Yong, "Harnessing complex fluid interfaces to control colloidal assembly and deposition," J. Colloid Interface Sci. **540**, 602–611 (2019).

[51] O. Aursjø and S. R. Pride, "Lattice Boltzmann method for diffusion-limited partial dissolution of fluids," Phys. Rev. E **92**, 013306 (2015).

[52] T. Scheel, P. Malgaretti, and J. Harting, "Enhancement of bubble transport in porous electrodes and catalysts," J. Chem. Phys. **160**, 194706 (2024).

[53] H. Liu, S. Sun, R. Wu, B. Wei, and J. Hou, "Pore-scale modeling of spontaneous imbibition in porous media using the lattice Boltzmann method," Water Resour. Res. **57**, e2020WR029219, https://doi.org/10.1029/2020wr029219 (2021).

[54] P. L. Bhatnagar, E. P. Gross, and M. Krook, "A model for collision processes in gases. I. Small amplitude processes in charged and neutral one-component systems," Phys. Rev. **94**, 511 (1954).

[55] T. Reis and T. N. Phillips, "Lattice Boltzmann model for simulating immiscible two-phase flows," J. Phys. A: Math. Theor. **40**, 4033 (2007).

[56] A. J. Ladd, "Numerical simulations of particulate suspensions via a discretized Boltzmann equation. Part 1. Theoretical foundation," J. Fluid Mech. **271**, 285–309 (1994).

[57] P. Virtanen, R. Gommers, T. E. Oliphant, M. Haberland, T. Reddy, D. Cournapeau, E. Burovski, P. Peterson, W. Weckesser, J. Bright, S. J. van der Walt, M. Brett, J. Wilson, K. J. Millman, N. Mayorov, A. R. J. Nelson, E. Jones, R. Kern, E. Larson, C. J. Carey, İ. Polat, Y. Feng, E. W. Moore, J. VanderPlas, D. Laxalde, J. Perktold, R. Cimrman, I. Henriksen, E. A. Quintero, C. R. Harris, A. M. Archibald, A. H. Ribeiro, F. Pedregosa, P. van Mulbregt, A. Vijaykumar, A. P. Bardelli *et al.*, "SciPy 1.0: Fundamental algorithms for scientific computing in Python," Nat. Methods **17**, 261–272 (2020).

[58] Q. Li, P. Zhou, and H. Yan, "Pinning–depinning mechanism of the contact line during evaporation on chemically patterned surfaces: A lattice Boltzmann study," Langmuir **32**, 9389–9396 (2016).

[59] Q. Zou and X. He, "On pressure and velocity boundary conditions for the lattice Boltzmann BGK model," Phys. Fluids **9**, 1591–1598 (1997).

[60] M. Hecht and J. Harting, "Implementation of on-site velocity boundary conditions for D3Q19 lattice Boltzmann simulations," J. Stat. Mech.: Theory Exp. **2010**, P01018.

[61] R. Hernandez-Perez, J. L. García-Cordero, and J. V. Escobar, "Simple scaling laws for the evaporation of droplets pinned on pillars: Transfer-rate-and diffusion-limited regimes," Phys. Rev. E **96**, 062803 (2017).